Journal of
Marine Science and Engineering

MDPI

Article

A Novel Sea Surface Roughness Parameterization Based on Wave State and Sea Foam

Difu Sun [1,2], Junqiang Song [1,2], Xiaoyong Li [1,2,*], Kaijun Ren [1,2] and Hongze Leng [1,2]

1 College of Meteorology and Oceanography, National University of Defense Technology, Changsha 410073, China; sundifu14@nudt.edu.cn (D.S.); junqiang@nudt.edu.cn (J.S.); renkaijun@nudt.edu.cn (K.R.); hzleng@nudt.edu.cn (H.L.)
2 College of Computer Science and Technology, National University of Defense Technology, Changsha 410073, China
* Correspondence: sayingxmu@nudt.edu.cn

Abstract: A wave state related sea surface roughness parameterization scheme that takes into account the impact of sea foam is proposed in this study. Using eight observational datasets, the performances of two most widely used wave state related parameterizations are examined under various wave conditions. Based on the different performances of two wave state related parameterizations under different wave state, and by introducing the effect of sea foam, a new sea surface roughness parameterization suitable for low to extreme wind conditions is proposed. The behaviors of drag coefficient predicted by the proposed parameterization match the field and laboratory measurements well. It is shown that the drag coefficient increases with the increasing wind speed under low and moderate wind speed conditions, and then decreases with increasing wind speed, due to the effect of sea foam under high wind speed conditions. The maximum values of the drag coefficient are reached when the 10 m wind speeds are in the range of 30–35 m/s.

Keywords: wind-wave interaction; momentum transfer; aerodynamic roughness; drag coefficient; wave state; sea foam

Citation: Sun, D.; Song, J.; Li, X.; Ren, K.; Leng, H. A Novel Sea Surface Roughness Parameterization Based on Wave State and Sea Foam. *J. Mar. Sci. Eng.* **2021**, *9*, 246. https://doi.org/10.3390/jmse9030246

Academic Editor: Lev Shemer

Received: 1 February 2021
Accepted: 22 February 2021
Published: 25 February 2021

1. Introduction

The momentum transfer between the atmosphere and the ocean plays an important role in the evolution of weather and climate [1–3]. Parameterization of the momentum transfer across the air–sea interface is essential to the modeling of many air–sea interaction activities, such as tropical cyclones and ocean waves [4]. In the current applications, the air–sea momentum flux τ is usually estimated from the drag coefficient C_d as follows:

$$\tau \equiv \rho u_*^2 = \rho C_d U_{10}^2, \quad (1)$$

where ρ is the air density, u_* is the friction velocity, and U_{10} is the wind speed at 10 m elevation above the sea surface. The logarithmic wind profile law can be expressed as [5–7]:

$$U_{10} = \frac{u_*}{\kappa}[ln(\frac{10}{z_0}) - \Psi_m(\frac{10}{L})], \quad (2)$$

where $\kappa = 0.4$ is the von Kármán constant, and z_0 is the sea surface aerodynamic roughness, Ψ_m is the stratification correction for the logarithmic wind profile, which is a function of the Obukhov length L, and the function of Ψ_m can be found in Paulson [8] for unstable stratification and in Grachev et al. [9] for stable stratification, respectively. By combining Equations (1) and (2), the relationship between C_d and z_0 is given as:

$$C_d = \kappa^2[ln(\frac{10}{z_0}) - \Psi_m(\frac{10}{L})]^{-2}. \quad (3)$$

Thus, there is an one-to-one correspondence between C_d and z_0 under a certain stratification, specifying that z_0 specifies C_d and vice versa. The sea surface aerodynamic roughness z_0 is widely used in the parameterization of the sea surface wind stress.

In current numerical models, C_d and z_0 are often parameterized as the function of wind speed U_{10}. In low and moderate wind conditions ($U_{10} \leq 20$ m/s), the results of many experiments show that C_d increases linearly with wind speed [10–13]. Thus, the function of C_d in low and moderate wind speed conditions can be expressed as [14]:

$$10^3 C_d = a + bU_{10}. \tag{4}$$

By fitting the coefficients a and b to observational data, different results were obtained from different studies (Table 1); the functions of C_d in low and moderate wind conditions from different research are qualitatively consistent, but differ significantly in values.

Table 1. Coefficients a and b in Equation (4) from different studies.

References	a	b
Kondo [15]	1.20	0.025
Smith and Banke [16]	0.63	0.066
Garratt [17]	0.75	0.067
Wu [18]	0.80	0.065
Large and Pond [19]	0.49	0.065
Donelan [20]	0.96	0.041
Geernaert et al. [12]	0.58	0.085
Yelland and Taylor [21]	0.60	0.070
Vickers and Mahrt [22]	0.75	0.067
Drennan et al. [23]	0.60	0.070
Guan and Xie [14]	0.78	0.065
Toffoli et al. [24]	0.96	0.060

Due to the lack of observational data in high wind speeds, the linear relationship between C_d and U_{10} in low and moderate winds has been extrapolated to high wind conditions in early applications, such as the modeling of tropical cyclones [25] and waves [26]. However, some recent experiments from both field and laboratory showed that C_d tends to saturate [27,28] or decrease [29,30] with wind speed at extremely high wind speeds. Therefore, in many recent applications of tropical cyclone [31,32] and storm surge modeling [33], the increasing value of C_d has been replaced by a constant that does not change with wind speed, or a value that decreases with increasing wind speed.

Several mechanisms of C_d saturation at high wind speeds from different aspects have been proposed, and a summary of them can be found in Bryant and Akbar [34]. Many researchers ascribed the reduction or saturation of the C_d to interface slipping and flattening accompanied by intense wave breaking at high wind speeds, which makes the wave steepness decrease or no longer increase, thereby affecting the aerodynamic roughness [35–37]. While some other researchers focused on the effect of sea foam on the momentum transfer process [38–40], the sea surface is covered by sea foam under high wind speed conditions, which changes the dynamics and thermodynamics of the air–sea interface. In addition to these two mechanisms, several other researchers explain the sea surface drag saturation from the unique airflow caused by breaking waves [41,42].

As the dependence of C_d on wind speed varies significantly (Table 1), the drag coefficient might depend not only on the wind speed [43]. Based on the above mentioned mechanisms of C_d saturation at high wind speeds, the dynamics and thermodynamics properties of the air–sea interface are crucial for the momentum transfer. Hence, it is convincible to parameterize the drag coefficient or the sea surface aerodynamic roughness through factors that describing the characteristic of the air–sea interface, i.e., wave age [44] and wave steepness [14].

Wave age and wave steepness are two of the most frequently used parameters to describe the air–sea interface and the development of wind wave. Wave age ($\beta = c_p/U_{10}$) is defined as the ratio between spectral peak phase velocity c_p and wind speed U_{10}, or replace U_{10} with friction velocity u_* ($\beta_* = c_p/u_*$). Wave age β denotes the relative speed of wave to wind, the smaller the β, the lower the wave relative to the wind, and thus the more momentum transferred from the air to the sea. Wave steepness ($\delta = H_s/L_p$) is defined as the ratio between significant wave height H_s and the wavelength at the spectral peak L_p, δ denotes the physical roughness of the sea surface. In general, β describes the relative magnitude of wave speed and wind speed, while δ describes the characteristic of roughness.

Due to the importance of wave state on the momentum transfer across the air–sea interface, many wave parameter based schemes have been proposed to improve the parameterization of the momentum transfer [12,45–47]. The dimensionless roughness z_0/H_s is often applied in the wave state related parameterization of the momentum transfer, as it has a stronger correlation with β and δ than the original C_d and z_0 [48]. Smith et al. [11], Donelan et al. [46], and Drennan et al. [49] have proposed their function of z_0/H_s based on β or β_*, respectively:

$$z_0/H_s = 1.33 \times 10^{-4}\beta^{-3.5}, \tag{5}$$

$$z_0/H_s = 1.68 \times 10^{-4}\beta^{-2.6}, \tag{6}$$

$$z_0/H_s = 3.35 \times \beta_*^{-3.4}. \tag{7}$$

These studies demonstrated a decreasing of the dimensionless roughness z_0/H_s with an increasing of wave age. On the other hand, Anctil and Donelan [50], Taylor and Yelland [51], and Takagaki et al. [28] have proposed their functions of z_0/H_s based on δ, respectively:

$$z_0/H_s = 6.39 \times 10^2\delta^{6.76}, \tag{8}$$

$$z_0/H_s = 1.2 \times 10^2\delta^{4.5}, \tag{9}$$

$$z_0/H_s = 10.94 \times \delta^{3.0}. \tag{10}$$

These studies demonstrate an increasing of the dimensionless roughness z_0/H_s with an increasing of wave steepness. The merits and limitations of both wave age based and wave steepness based sea surface roughness parameterization have been examined in several studies. Among them, the wave steepness based scheme proposed by Taylor and Yelland [51] (see Equation (9), hereafter TY01) and the wave age based scheme proposed by Drennan et al. [49] (see Equation (7), hereafter DN03) have received the most attention [48,52,53]. In general, the wave state related parameterizations present a better performance than the wind speed related bulk parameterizations, wave age based and wave steepness based schemes showed advantages in different wind or wave conditions, but none of them showed a good performance in all situations.

In addition to the wave state, sea foam also has a significant effect on the dynamics and thermodynamics properties of the air–sea interface. Under high wind conditions, the impact of sea foam on momentum transport cannot be ignored [54]. Owing to the lack of observational wave data under high wind conditions ($U_{10} \geq 25$ m/s), the aforementioned wave state related parameterizations have been proposed based only on the observational wave data under low to moderate wind speeds ($U_{10} \leq 20$ m/s). Note that, since the impact of sea foam on sea surface is minimal at low to moderate wind speeds [38,55], the effect of sea foam has not been included in these parameterizations implicitly.

In this study, we have evaluated the performance of two most widely used wave state related parameterizations (TY01 and DN03), using a combination of eight datasets including various wind and wave conditions. Based on the advantages and limitations of two schemes in different conditions, we propose a new wave state related parameteration scheme, by adding the effect of sea foam to the momentum transfer for existing schemes, which is verified to be suitable for low to extreme wind conditions ($U_{10} > 40$ m/s).

The paper is organized as follows: Section 2 describes the observational datasets used to evaluate the performance of two wave state related parameterizations. Based on the different performances of two wave state related parameterizations under different wave states, a combination of them is proposed in Section 3. Section 4 introduces the effect of sea foam into the scheme presented in Section 3; thus, the new parameterization of sea surface roughness based on the wave state and sea foam is proposed. C_d predicted by the new parameterization under high wind speed conditions is verified by the observational data in Section 5. Finally, Section 6 gives a summary of this study.

2. Datasets

To examine the performance of two most widely used wave state related parameterization: wave age based DN03 and wave steepness based TY01, eight observational datasets (published in tabular form) were used in this study. Wind stress in seven datasets was calculated using the direct eddy-correlation (EC) method [56] and the other dataset adopted the inertial dissipation (ID) method [57]. These datasets are described below, and a summary of them is given in Table 2.

a. Lake Ontario

The Lake Ontario dataset was collected from the air–sea interaction experiment conducted in the western basin of Lake Ontario in the autumn of 1994 and 1995. A sonic anemometer was deployed on a 7.8 m-height bow mast to measure the wind fluctuations, which were used to calculate wind stress, and the sampling time of each run was 80 min (by pooling four consecutive 20-min averages groups to reduce the sampling error). Wave information was measured using a wave staff array. Here, we use the Lake Ontario data published by Anctil and Donelan [50].

b. AUSWEX

The Australian Shallow Water Experiment (AUSWEX) took place in the eastern basin of Lake George in 1997–2000 [58]. Two anemometer masts, accommodating wind probes, were mounted at 10-m height. Wind stress was calculated using the 21-Hz velocity data measured from an ultrasonic anemometer. Wave data were measured using eight wave probes. Here, we use the AUSWEX data published by Babanin et al. [59].

c. ERS Validation

The wind stress and wave data in this dataset were the validation data for the Grand Banks Earth Remote Sensing Satelite (ERS-1) Synthetic Aperture Radar (SAR) Wave Validation Experiment, which was collected from the scientific ship *Hudson* in the open North Atlantic. Wind data were measured using an anemometer system deployed on the bow of the ship, and the height of the system was 14 m. Wave data were measured using three wave buoys. Data used in this study were published by Dobson et al. [60].

d. SWADE

The data presented by Drennan et al. [61] were taken as part of the Surface Waves Dynamics Experiment (SWADE), which was conducted in 1990–1991 off the coast of Virginia. A 20-m swath ship was deployed to provide a high-resolution measurements near the air–sea interface [62]. Wind fluctuations were measured from an 12-m height anemometer, from which the wind stress was calculated, the sampling time was 17 min. Wave information was obtained using a wave staff array.

e. FPN

The North Sea Platform (FPN) experiment in 1985 was carried out on a platform located 65 km southwest of West Strand. Wind fluctuations were measured using a 33-m height sonic anemometer to calculate wind stress, and the sampling time was 30 min. Wave data were collected by a rider buoy located 800 m southwest of the platform, and were recorded on the platform. Data used in our study were released by Geernaert et al. [12] in tabular form.

f. HEXOS

The Humidity Exchange over the Sea (HEXOS) experiment was carried out on the Dutch research platform *Meetpost Noordwijk* (MPN) in the autumn of 1986. Wind fluctuations were obtained using a sonic and a pressure anemometer concurrently to calculated wind stress, height of them was 6 m, data collected from the pressure anemometer were adopted in this study, the sampling time for each run was 20 min. Wave data were collected by a rider buoy which was 150 m away from the platform. Here, we use the HEXOS data published by Janssen et al. [63].

g. RASEX

The Risø Air–Sea Exchange (RASEX) field experiment was performed at a shallow-water site near Denmark. In this experiment, wind fluctuation data were obtained from a 3 m height sonic anemometer, accompanied by the mean wind speed data collected from a cup anemometer located at 7 m, the sampling time for each run was 30 min. Wave data were gathered from the wave gauge near the tower. Data used here were obtained from Johnson et al. [64].

h. GOTEX

The Gulf of Tehuantepec Experiment (GOTEX) was carried out in February 2004. Data used in this study were presented by Romero and Melville [65], which were obtained from the National Science Foundation/National Center for Atmospheric Research (NSF/NCAR) C-130 aircraft. Vector winds were measured by the airborne detector at 25 Hz frequency, from which wind stress was calculated [66]. Frictional velocity u_* was estimated from the lowest-height runs (about 40 m above the water surface) with a time average of 50 s. The sea surface elevation data were measured using a lidar system.

Table 2. Summary of eight datasets. The method EC denotes the wind stress was measured using direct eddy-correlation method, ID denotes the inertial dissipation method.

Dataset	**Lake Ontario**	**AUSWEX**	**ERS Validation**	**SWADE**
Reference	Anctil and Donelan [50]	Babanin et al. [59]	Dobson et al. [60]	Drennan et al. [61]
Platform	tower	suspended bridge	ship	ship
Location	Lake Ontario	Lake George	North Atlantic	Atlantic shelf
Method	EC	EC	ID	EC
Height	7.8 m	10 m	14 m	12 m
Sampling time	80 min	10 min	10∼30 min	17 min
Dataset	**FPN**	**HEXOS**	**RASEX**	**GOTEX**
Reference	Geernaert et al. [12]	Janssen et al. [63]	Johnson et al. [64]	Romero and Melville [65]
Platform	FPN platform	MPN platform	tower	aircraft
Location	North Sea	North Sea	Baltic coast	Gulf of Tehuantepec
Method	EC	EC	EC	EC
Height	33 m	6 m	7 m	about 40 m
Sampling time	30 min	20 min	30 min	50 s

In several datasets, the wavelength at the spectral peak L_p was not measured directly. We calculate it using the dispersion relationship:

$$\omega^2 = gk\tanh kh, \quad (11)$$

where ω is the angular frequency, g is the gravitational acceleration, k is the wavenumber, and h denotes the depth of water. For deep water ($h > \frac{L}{2}$, where L is the wavelength), L_p can be calculated from:

$$L_p = \frac{gT_p^2}{2\pi}, \tag{12}$$

where T_p denotes the period of wave at the spectral peak. If deep water conditions are not met, by substituting $\omega = 2\pi/T_p$ and $k = 2\pi/L_p$ into Equation (11), L_p can be calculated from T_p and h. When both T_p and f_p (frequency of wave at the spectral peak) were not presented by the dataset, T_p can be determined using the equations developed by Carter [67], which were derived from the Joint North Sea Wave Project (JONSWAP). For fetch limited seas:

$$T_p = 0.566X^{0.3}U_{10}^{0.4}, \tag{13}$$

where X is the fetch in kilometers. For duration limited seas:

$$T_p = 0.540D^{3/7}U_{10}^{4/7}, \tag{14}$$

where D is the duration in hours.

In addition to eight wind and wave datasets measured in low and moderate wind conditions, four datasets of C_d in high wind speed conditions are also used in the validation of our new sea surface roughness parameterization in Section 5, two of them are field observations: Powell et al. [29] and Jarosz et al. [68], and the other two are laboratory observations: Donelan et al. [27] and Takagaki et al. [28]. Here, we make a brief introduction to them.

Powell et al. [29] measured the wind profile in tropical cyclone boundary layer using Global Positioning System, from the intercept and slope of the wind profile, C_d and z_0 for winds up to 50 m/s are measured.

Due to the difficulties of direct stress measurements at high wind speeds caused by the spray droplets and the damages of winds to the instruments, Jarosz et al. [68] estimated the air–sea momentum transfer from the ocean side, namely the bottom-up method [27]. Using currents' observations recorded by the Acoustic Doppler current profiler during Hurricane Ivan, C_d is calculated from:

$$C_d = \frac{\rho_w h}{\rho U_{10} U_{10x}}\left(\frac{\partial U_w}{\partial t} - fV_w + \frac{rU_w}{h}\right) \tag{15}$$

where ρ_w and ρ are the density for water and air, respectively; f is the Coriolis parameter; U_w and V_w are the depth-integrated along and across the continental shelf current velocity components, respectively; U_{10x} is the along-shelf component of 10 m wind speed; and r is a constant resistance coefficient at the sea floor, which describes the degree of the bottom friction, and it usually ranges from 0.0001 cm/s to 0.1 cm/s. Using the bottom-up method, C_d is estimated under different r for winds between 20 and 48 m/s.

Donelan et al. [27] measured C_d in laboratory conditions for winds up to 53 m/s using the Air–Sea Interaction Facility at the University of Miami, three methods were compared in the calculation of C_d: momentum budget (MB), profile method (PM), and Reynolds stress (RS), the results from which were only slightly different. Tools for measuring stress include hot-film anemometry, digital particle image velocimetry (DPIV), and laser/line scan cameras for measuring the water surface elevation.

Using a high-speed wind-wave tank, Takagaki et al. [28] measured C_d and z_0 for winds up to 64 m/s from wind velocity components collected by laser Doppler and phase Doppler anemometers; the eddy correlation method was utilized in their measurements to calculate C_d and z_0.

3. Evaluation of Two Wave State Related Parameterizations

The dimensionless roughness z_0/H_s of data points from eight datasets are plotted in Figure 1a against wave steepness δ, the curve of TY01 is also shown as the solid line.

It is shown that TY01 is able to describe the positive correlation between z_0/H_s and δ in general, but the data points are quite scattered.

For comparison, we plot the same data points using the wave age scaling in Figure 1b, i.e., z_0/H_s versus β_*. The curve of DN03 provides a better prediction of the dimensionless roughness z_0/H_s than TY01, the data points are more concentrated near the curve than in Figure 1a.

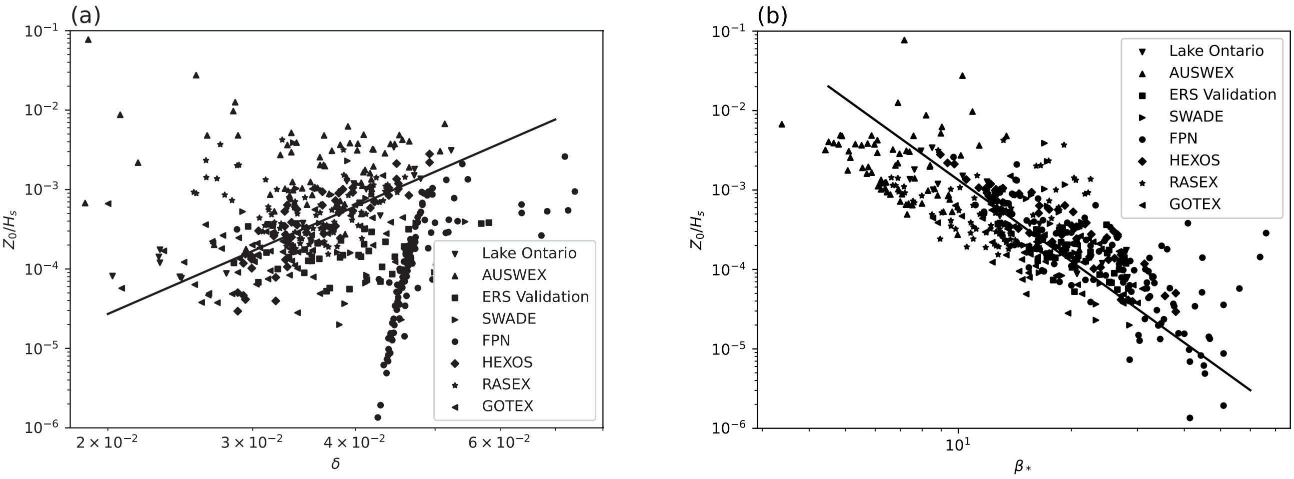

Figure 1. Dimensionless roughness z_0/H_s vs. (**a**) wave steepness δ and (**b**) wave age β_* for data points from eight datasets. The solid lines represent the curves of TY01 and DN03 in (**a**,**b**), respectively.

Although the plots of dimensionless roughness z_0/H_s for all data points show the overall performance of two parameterizations, it is more instructive to test how they predict the drag coefficient. z_0 can be converted to C_d by Equation (3). A comparison between measured and predicted C_d has been made for each dataset, and the results of TY01 and DN03 are presented in Figures 2 and 3, respectively. Note that the data points that fall within the 90% confidence regions are denoted as black points.

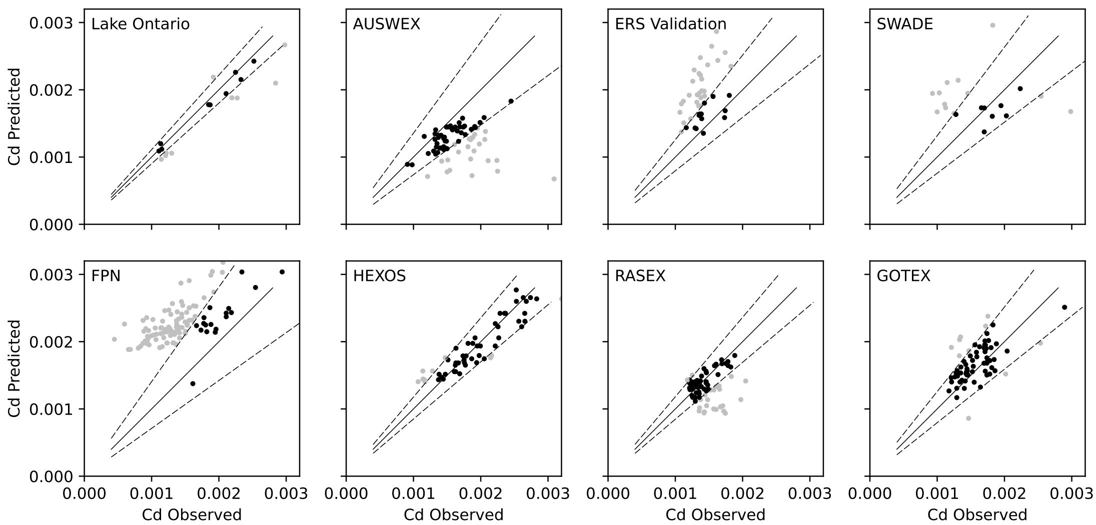

Figure 2. Measured drag coefficient vs. the value predicted by TY01 for eight datasets. Data points fall within the 90% confidence regions are shown in black points, and data points falling outside the 90% confidence regions are shown in grey points. Solid lines indicate the best fit between observations and predictions. Dashed lines represent the upper and lower boundaries of the 90% confidence regions.

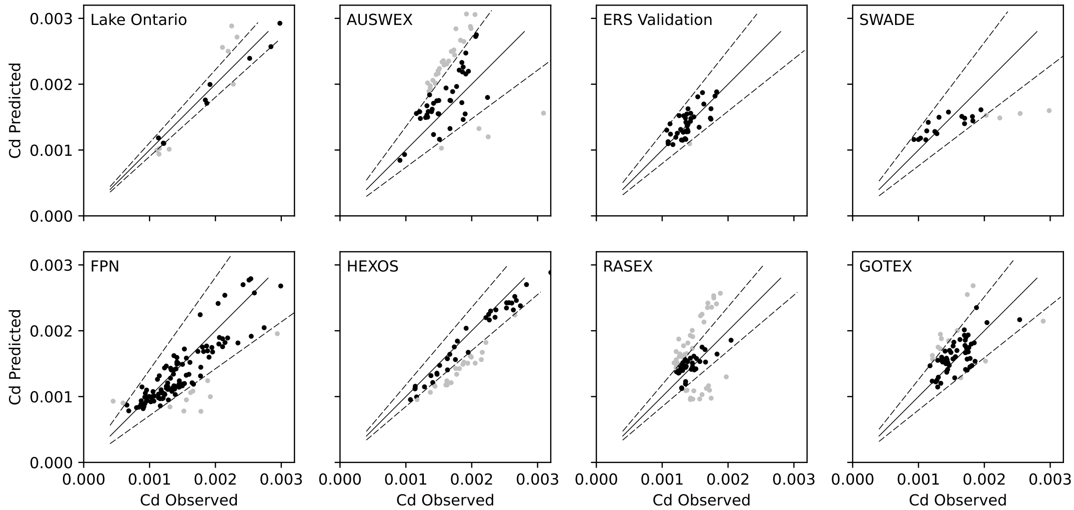

Figure 3. Measured drag coefficient vs. the value predicted by DN03 for eight datasets. Data points fall within the 90% confidence regions are shown in black points, and data points fall outside the 90% confidence regions are shown in grey points. Solid lines indicate the best fit between observations and predictions. Dashed lines represent the upper and lower boundaries of the 90% confidence regions.

The 90% confidence regions for datasets using the EC method are calculated based on the sampling errors ε [69], where the sampling errors of six EC datasets can be calculated following Donelan [70]:

$$\varepsilon = 9.2z^{1/2}(UY)^{-1/2}, \tag{16}$$

where Y is the sampling time (s), U is the mean wind speed for an experiment, and z is the height of the anemometer above the water level. The sampling errors of eight datasets are summarized in Table 3. It is worth mentioning that the wind stress in the ERS Validation dataset was calculated using the ID method, Equation (16) is not applicable, and, following Drennan et al. [52], we assume an error equal to the mean sampling error of the EC data (25.77%). Similarly, data from GOTEX were collected from the aircraft, and the measuring instrument and post-processing method were inconsistent from other datasets. Equation (16) is suitable mainly for traditional platforms, i.e., buoy and tower. Thus, the sampling error for GOTEX dataset was also assumed as the mean sampling error for the EC data (25.77%).

In Figures 2 and 3, the 90% confidence regions are shown as the areas between the dotted lines, and the slope of the upper and the lower boundary line is $1 + \varepsilon$ and $1/(1 + \varepsilon)$, respectively. To evaluate the performance of TY01 and DN03 quantitatively, P_{90} was defined as the percentage of data points that fall within the 90% confidence regions. The normalized bias (NB) is defined as:

$$NB = \frac{\sum(X_{mod} - X_{obs})}{\sum X_{obs}}, \tag{17}$$

and the normalized root-mean-square-error ($NRMSE$) is defined as:

$$NRMSE = \sqrt{\frac{\sum(X_{obs} - X_{mod})^2}{\sum X_{obs}^2}}, \tag{18}$$

where X_{obs} is the observation, and X_{mod} is the corresponding value calculated from parameterization schemes [71]. In addition, P_{90}, NB, and $NRMSE$ predicted by TY01 and DN03 for each dataset are shown in Table 4, also shown are the mean β, mean β_*, and mean δ for each dataset. From Table 4, we can see that the correlation between P_{90} and NB or $NRMSE$ is strong, and datasets with larger P_{90} tend to have smaller NB and $NRMSE$, and datasets in which TY01 performs better under P_{90} are consistent with that under $NRMSE$. Considering that P_{90} is consistent with NB and $NRMSE$ qualitatively, and has the advantage of being able to take into account the sampling error of each dataset, we mainly focus on P_{90} in the following analysis.

Table 3. Sampling errors of eight datasets.

Dataset	Height (m)	Mean Wind Speed (m/s)	Sampling Time (s)	Number of Data	Sampling Error
Lake Ontario	7.8	11.39	4800	18	10.99%
AUSWEX	10	11.15	600	71	35.57%
ERS Validation	-	-	-	41	25.77%
SWADE	12	9.90	1020	20	31.71%
FPN	33	9.43	1800	116	40.57%
HEXOS	6	13.56	1200	58	17.67%
RASEX	7	10.05	1800	80	18.10%
GOTEX	-	-	-	67	25.77%

The sampling errors of the ERS validation dataset and the GOTEX dataset were assumed as the mean sampling error of six other datasets.

Table 4. P_{90}, NB, and $NRMSE$ predicted by TY01 and DN03 for each dataset.

Dataset	Mean β	Mean β_*	Mean δ	P_{90}-TY01	P_{90}-DN03
Lake Ontario	0.6542	16.69	0.0354	**0.5000**	**0.5000**
AUSWEX	0.2978	7.54	0.0367	**0.6620**	0.5493
ERS Validation	0.7984	20.89	0.0392	0.3171	**0.9756**
SWADE	0.7487	18.88	0.0405	0.4000	**0.8000**
FPN	0.9917	27.43	0.0481	0.1638	**0.9052**
HEXOS	0.8007	19.20	0.0362	**0.7931**	0.6379
RASEX	0.4798	12.68	0.0352	**0.6875**	0.4625
GOTEX	0.6977	17.69	0.0329	**0.8507**	0.8060
Total	0.6948	18.18	0.0390	0.5393	**0.7155**
Dataset	***NB*-TY01**	***NB*-DN03**	***NRMSE*-TY01**	***NRMSE*-DN03**	
Lake Ontario	−0.0847	**−0.0003**	**0.1330**	0.1346	
AUSWEX	−0.2587	**0.2120**	**0.3447**	0.3734	
ERS Validation	0.3727	**0.0059**	0.4377	**0.1101**	
SWADE	0.1514	**−0.1241**	0.3990	**0.2796**	
FPN	0.6924	**−0.0938**	0.7757	**0.1985**	
HEXOS	**−0.0107**	−0.1125	**0.1089**	0.1358	
RASEX	−0.0828	**0.0790**	**0.1931**	0.2603	
GOTEX	0.0684	**0.0517**	**0.1839**	0.1857	
Total	0.1464	**0.0090**	0.4327	**0.2302**	

Schemes with better performance under different indicators are bolded.

We first consider the results predicted by TY01 shown in Figure 2 and Table 4. TY01 is seen to work well for the AUSWEX, HEXOS, RASEX, and GOTEX datasets with a P_{90} larger than 0.65, but C_d measured in ERA Validation, SWADE, and FPN datasets was poorly predicted with a P_{90} less than 0.4, especially in the FPN dataset ($P_{90} = 0.1638$). As we can see from Figure 2, C_d in ERS Validation and FPN datasets were extremely overpredicted by TY01, it is worth noticing that the mean β_* of ERS Validation and FPN datasets were the largest two among eight datasets (both larger than 20), corresponding to a mature wave field. Moreover, TY01 underpredicted C_d from AUSWEX and RASEX datasets, whose mean β_* was the smallest two among eight datasets. The performance of TY01 shows an obvious sensitivity to β_*; for datasets having a larger β_*, TY01 tend to overpredict C_d from them; but, for datasets having a smaller β_*, C_d from them was underpredicted.

The results of DN03 were shown in Figure 3 and Table 4. The overall performance of DN03 is better than TY01. The results of DN03 from ERS Validation, SWADE, and FPN datasets are much better than TY01, but C_d measured in AUSWEX, HEXOS, and RASEX was poorly predicted and worse than TY01. For datasets in which DN03 performs well, the mean β_* was seen to be large (20.89, 18.88, 27.43, and 17.69 for ERS Validation, SWADE, FPN, and GOTEX, respectively), and in two datasets that have a smaller β_* (7.54 for AUSWEX and 12.68 for RASEX), the performance of DN03 is quite worse. Therefore, the performance of DN03 also shows a sensitivity to β_*.

In order to analyze the applicability of TY01 and DN03 in different conditions, we examine the sensitivity of their performance to β, β_*, and δ. Here, we use TY01_in to denote the data points predicted by TY01 that fall within the 90% confidence regions, corresponding to those data accurately predicted by TY01; and TY01_out to denote the data points predicted by TY01 that fall outside the 90% confidence regions, corresponding to those data that are not accurately predicted by TY01. DN03_in and DN03_out are the same, but for data points predicted by DN03. Table 5 shows the mean β, mean β_*, and mean δ of TY01_in, TY01_out, DN03_in, and DN03_out.

The mean β and β_* of TY01_in is much smaller than that of TY01_out, demonstrating that TY01 tends to have better performance at younger wave conditions. The mean δ of TY01_in is close to the mean δ of TY01_out, indicating that the performance of TY01 is not sensitive to δ. The difference of the mean β between DN03_in and DN03_out is not as obvious as between TY01_in and TY01_out, but the difference of the mean β_* between DN03_in and DN03_out is non-negligible. The difference of the mean δ between DN03_in and DN03_out is not obvious, demonstrating that the performance of DN03 is also not sensitive to the wave steepness.

Table 5. Sensitivities of the performance of TY01 and DN03 to β, β_*, and δ.

	Mean β	**Mean β_***	**Mean δ**
TY01_in	0.5873	14.60	0.0369
TY01_out	0.8206	22.38	0.0414
DN03_in	0.7205	19.08	0.0398
DN03_out	0.6302	15.93	0.0369

Considering that the performance of TY01 and DN03 is both sensitive to β_*, to further investigate the sensitivities of the performance of TY01 and DN03 to β_*, we divide the 471 data from eight datasets into 10 groups of roughly equal numbers (47 or 48 per group) according to β_* from low to high, and calculate the P_{90} of each group, the results are shown in Table 6. Changes in performance of TY01 and DN03 with β_* are clearly demonstrated, when β_* exceeds 16, the performance of TY01 drops significantly; when β_* is smaller than 10, the performance of DN03 is relatively poor. Considering the different performance of TY01 and DN03 in different conditions, it is reasonable to combine them by using TY01 in small β_* conditions and using DN03 in large β_* conditions. Another issue is the choice of the demarcation point between TY01 and DN03, since the datasets used in this study do not cover all wind and wave conditions, and there are inconsistencies between datasets due to different observation and processing methods, we cannot determine the demarcation points arbitrarily as the point where the performance of DN03 exceeds TY01. Therefore, we use the $\delta - \beta_*$ relationship derived from *Toba's* [72] 3/2 power law to determine the demarcation points between TY01 and DN03. The well-known 3/2 power law is given as:

$$H_* = BT_*^{3/2}, \tag{19}$$

where $H_* = gH_s/u_*^2$ and $T_* = gT_s/u_*$ are non-dimensional significant wave height and period, and $B = 0.062$ is a constant. The 3/2 power law has been verified by many studies [64,73,74], which is suitable for low to extreme wind conditions [48]. Multiplying Equation (19) by $2\pi u_*^2/g^2T_p^2$, we get:

$$\frac{2\pi H_s}{gT_p^2} = 2\pi \times 0.062(\frac{gT_p^4}{u_* T_s^3})^{-1/2}, \tag{20}$$

by using the relation between significant wave period T_s and peak wave period T_p [75,76]:

$$T_s = 0.91T_p, \tag{21}$$

and by calling the relation $c_p = gT_p/2\pi$, Equation (20) can be rewritten as:

$$\delta = 0.135\beta_*^{-1/2}. \tag{22}$$

By combining Equation (7) (function of DN03), Equation (9) (function of TY01), and Equation (22), we work out that the curves of TY01 and DN03 intersect at $\beta_* = 15.21$. According to the above inference, $\beta_* = 15.21$ is selected as the demarcation point between TY01 and DN03, TY01 is adopted when $\beta_* < 15.21$, and DN03 is adopted when $\beta_* \geq 15.21$:

$$z_0/H_s = \begin{cases} 1.2 \times 10^2\delta^{4.5}, & \beta_* < 15.21 \\ 3.35 \times \beta_*^{-3.4}, & \beta_* \geq 15.21 \end{cases}. \tag{23}$$

Table 6. P_{90} of 10 groups divided according to β_* from low to high.

Groups with Different β_* Ranges	P_{90}-TY01	P_{90}-DN03
Group 1 ($3.38 \leq \beta_* \leq 7.24$)	**0.7083**	0.3125
Group 2 ($7.26 \leq \beta_* \leq 9.95$)	**0.7021**	0.6170
Group 3 ($10.02 \leq \beta_* \leq 12.54$)	**0.6596**	**0.6596**
Group 4 ($12.59 \leq \beta_* \leq 13.75$)	0.7447	**0.8085**
Group 5 ($13.78 \leq \beta_* \leq 16.12$)	0.6809	**0.8298**
Group 6 ($16.13 \leq \beta_* \leq 18.36$)	0.5106	**0.8085**
Group 7 ($18.43 \leq \beta_* \leq 20.78$)	0.4894	**0.7447**
Group 8 ($20.79 \leq \beta_* \leq 25.59$)	0.4894	**0.8085**
Group 9 ($25.70 \leq \beta_* \leq 31.33$)	0.4043	**0.7872**
Group 10 ($31.40 \leq \beta_* \leq 66.10$)	0.0000	**0.7660**

Schemes with better performance are bolded.

To verify the validity of the combination of TY01 and DN03 given in Equation (23), Figure 4 plotted a comparison between the measured C_d and the corresponding values predicted by Equation (23) as in Figures 2 and 3. By comparing Figures 2 and 4, we can see that the performance of the combined scheme is much better than that of TY01, especially in ERS Validation and FPN datasets. By comparing Figures 3 and 4, the improvement of the combined scheme compared to DN03 mainly comes from the RASEX dataset; most of the RASEX data overestimated by DN03 have been improved in the combined scheme. We further compared the P_{90}, NB, and $NRMSE$ predicted by TY01, DN03, and the combined scheme for the total eight datasets (Table 7); the results show that the performance of the combined scheme is much better than TY01 in P_{90} and $NRMSE$, and slightly better than that of DN03, NB predicted by the combined scheme is slightly worse than DN03. Considering that NB mainly describes the overestimation or underestimation of the prediction, and can be offset if both overestimation and underestimation exist, while P_{90} and $NRMSE$ are the key parameters to show the overall performance; the results in Table 7 prove that the performance of the combined scheme is better than TY01 and DN03.

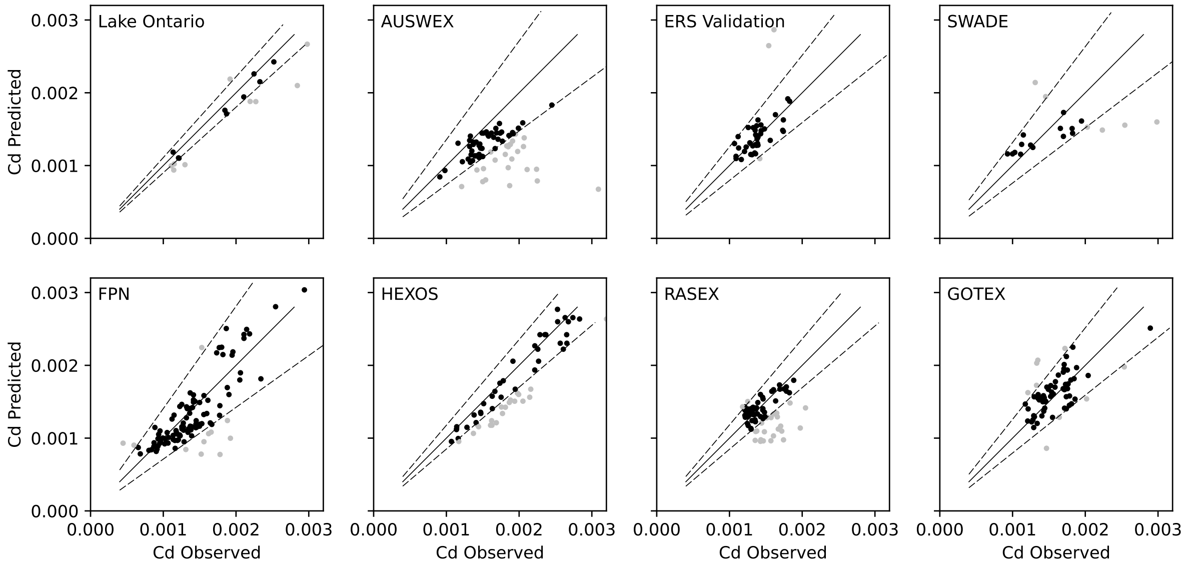

Figure 4. Measured drag coefficient vs. the value predicted by Equation (23) for eight datasets. Data points fall within the 90% confidence regions are shown in black points, and data points fall outside the 90% confidence regions are shown in grey points. Solid lines indicate the best fit between observations and predictions. Dashed lines represent the upper and lower boundaries of the 90% confidence regions.

Table 7. P_{90}, NB, and $NRMSE$ predicted by TY01, DN03, and the combined scheme (Equation (23)) for the total eight datasets.

	TY01	DN03	Combined
P_{90}	0.5393	0.7155	**0.7537**
NB	0.1464	**0.0090**	0.0496
$NRMSE$	0.4327	0.2302	**0.2249**

Schemes with better performance are bolded.

4. Effect of Sea Foam

TY01 was developed using three datasets: HEXOS, RASEX, and Lake Ontario, and DN03 was developed using the pure wind sea subsets of five datasets: AGILE (measured from the 15-m research vessel *AGILE*) [77], FETCH (Flux, sea state and remote sensing in conditions of variable fetch) [78], HEXOS, SWADE, and WAVES (Water–Air Vertical Exchange Study) [79]; these datasets were collected under low and moderate wind conditions ($U_{10} \leq 20$ m/s). Compared to low and moderate wind conditions, a significant change in high wind conditions ($U_{10} \geq 25$ m/s) is the generation of sea foam due to intense wave breaking, which plays an important role in the leveling off or decrease of C_d and z_0. Since the effect of sea foam on sea surface roughness is minimal at low to moderate wind speeds [38,55], the effect of sea foam was not implicitly included in the proposing of TY01 and DN03, and an introduction of the effect of sea foam to TY01 and DN03 will enhance their applicability for high wind speed conditions.

A semi-empirical model is proposed by [55] to estimate the influence of sea foam on aerodynamic roughness. Their model treats the effective air–sea aerodynamic roughness (z_{eff}) as the weighted sum of two parts: one is the foam-free (z_n) part and the other is the foam-covered (z_f) part. The average z_{eff} under area S is assumed as follows:

$$z_{eff} = \frac{1}{S}\left(\int_{S_n} z_n dS' + \int_{S_f} z_f dS'\right). \tag{24}$$

Here, $S = S_n + S_f$ is the total area, in which S_n and S_f are the foam-free and foam-cover areas, respectively. Thus, Equation (24) can be rewritten as:

$$z_{eff} = \frac{S - S_f}{S} z_n + \frac{S_f}{S} z_f, \tag{25}$$

by defining $\alpha_f = S_f/S$ as the fractional foam coverage, we obtain:

$$z_{eff} = (1 - \alpha_f) z_n + \alpha_f z_f. \tag{26}$$

The fractional foam coverage α_f is highly related to U_{10} [80]. The function between α_f and U_{10} can be approximated from the observational data as in Holthuijsen et al. [80]:

$$\alpha_f = \gamma \tanh[\alpha \exp(\zeta U_{10})], \tag{27}$$

with $\alpha = 0.00255$, $\zeta = 0.166$, and $\gamma = 0.98$. To demonstrate the different patterns of α_f in different situations, a universal dimensionless form of Equation (27) is given as:

$$\alpha_f = \gamma \tanh[\alpha \exp(\tilde{\zeta} \frac{U_{10}}{U_{10}^{(s)}})], \tag{28}$$

where $\tilde{\zeta} = 8$, $U_{10}^{(S)}$ is the saturation speed, defined as the value where the difference between α_f and its saturation limit $\alpha_f = 1$ is less than 2%. The curve of foam coverage α_f versus U_{10} from Equation (28) varies and $U_{10}^{(S)}$ is presented in Figure 5, the results show that, when the wind speed U_{10} exceeds 40 m/s, the foam coverage α_f is very close to 0.98, while α_f is minimal when U_{10} is less than 20 m/s. Observational data collected from the open ocean by Holthuijsen et al. [80] suggest a value of $U_{10}^{(S)} = 48$ m/s. According to the open-ocean experimental data for C_d or, alternatively, z_{eff} [29], it is assumed that the minimum value for $C_d = 0.0017$ or, $z_{eff} = 0.0003$ m is reached at the same wind speed $U_{10} = 48$ m/s (see Figures 2 and 3 in Golbraikh and Shtemler [55]). Because the relation between C_d and U_{10} in laboratory conditions is quite different from that of the open ocean, Golbraikh and Shtemler [55] suggested a different minimum value for z_{eff} in laboratory conditions, which is $z_{eff} = 0.0028$ m. Then, we adopt $U_{10} = 48$ m/s as the saturation velocity, and the minimum value of $z_{eff} = 0.0003$ m as the foam-covered aerodynamic roughness z_f in Equation (26) for open ocean conditions, and the minimum value of $z_{eff} = 0.0028$ m for laboratory conditions. As the effect of sea foam was not implicitly included in the proposing of TY01 and DN03, the aerodynamic roughness predicted by Equation (23) can be taken as the foam-free aerodynamic roughness z_n in Equation (26), substituting Equation (23) into Equation (26), a new parameterization of sea surface roughness including the impact of sea foam is obtained:

$$z_0/H_s = \begin{cases} (1-\alpha_f)1.2 \times 10^2 \delta^{4.5} + \alpha_f z_f/H_s, & \beta_* < 15.21 \\ (1-\alpha_f)3.35 \times \beta_*^{-3.4} + \alpha_f z_f/H_s, & \beta_* \geq 15.21 \end{cases}, \tag{29}$$

where z_0 is the aerodynamic roughness, δ is wave steepness, β_* is wave age, H_s is the significant wave height, α_f is the foam coverage (calculated from Equation (28)), and z_f is the foam-covered aerodynamic roughness (taken as 0.0003 m for open ocean conditions, and 0.0028 m for laboratory conditions in this study). By combining TY01 and DN03 in the form of a piecewise function, the new proposed parameterization is able to make better predictions of z_0 in various wind and wave conditions. By adding the impact of sea foam, the predictions of z_0 in high wind speed conditions are improved.

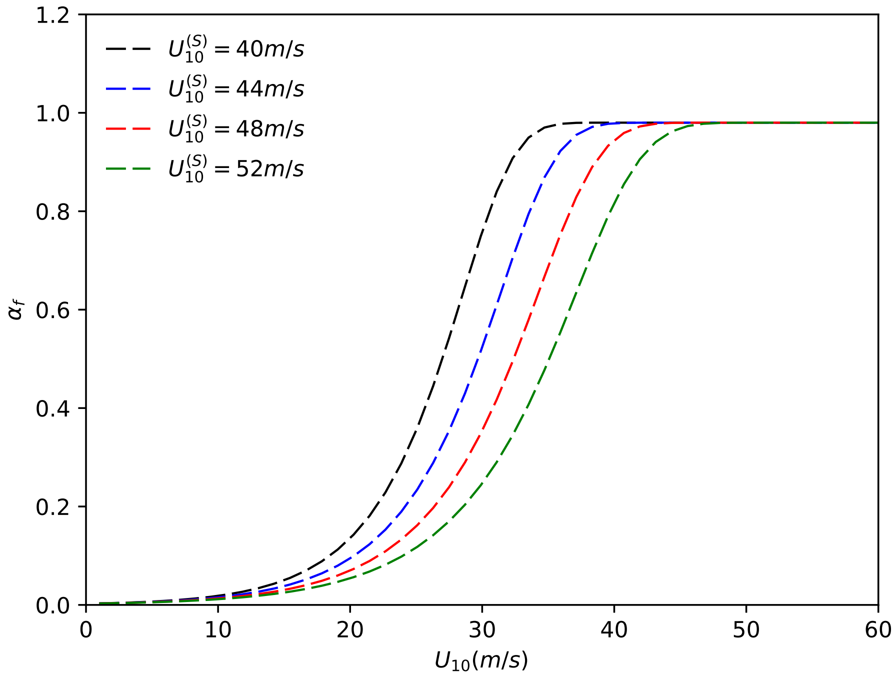

Figure 5. The foam coverage α_f versus U_{10} from Equation (28) in different $U_{10}^{(S)}$.

5. Validation and Discussion

As aforementioned, the proposed parameterization calls TY01 and DN03 according to different wave ages; its comparison against observations in low and moderate wind conditions have been made in Section 3. In this section, we will make a brief validation on the behavior of C_d predicted by the proposed parameterization under high wind speed conditions. Specifically, datasets from several recent experiments [27–29,68] with observations under high wind speed conditions are compared with the new parameterization.

5.1. Estimation of H_s

These observational data were presented in the form of C_d vs. U_{10}, in order to compare the proposed parameterization with these observational data; it is essential to parameterize H_s with U_{10}.

Several schemes were proposed for the parameterization of H_s. From the formulas for fully developed wave field in deep water, Taylor and Yelland [51] proposed a parameterization of H_s:

$$H_s = 0.0248U_{10}^2. \tag{30}$$

According to Equation (30), Fairall et al. [81] developed an empirical formula for predicting H_s in the Coupled Ocean-Atmosphere Response Experiment bulk algorithm (COARE 3.0):

$$H_s = 0.018U_{10}^2(1 + 0.015U_{10}). \tag{31}$$

In addition, using 15 years of hourly buoy data, Wang et al. [82] developed a H_s scheme for open oceans:

$$H_s = 0.0143U_{10}^2 + 0.9626. \tag{32}$$

These schemes all reveal the monotonically increasing of H_s with U_{10}, and this trend has been verified in low and moderate wind speeds, their applicability in high wind speed conditions is doubtful. The plots of H_s versus U_{10} of the three schemes above are shown in Figure 6a, the values of H_s from three schemes are relatively reasonable at low and moderate wind speeds; however, as the wind speed increases, H_s becomes unreasonably large, the values of H_s calculated from three schemes all exceed 50 m at $U_{10} = 60$ m/s, which are obviously unreasonable. However, accurate prediction of H_s under high wind speeds requires the help of numerical models. Considering that our purpose is only to get the brief relationship between H_s and U_{10}, we simply add a threshold of 21 m to H_s to replace the unreasonably large value under high wind speeds (Figure 6b). The value of 21 m comes from the largest H_s measured by the radar altimeter onboard the Jason 2 satellite (http://cersat.ifremer.fr/user-community/news/item/346-record-breaking-wave-heights-and-periods-in-the-north-atlantic, accessed on 11 February 2021) which is 20.1 m; here, we round it to 21 m.

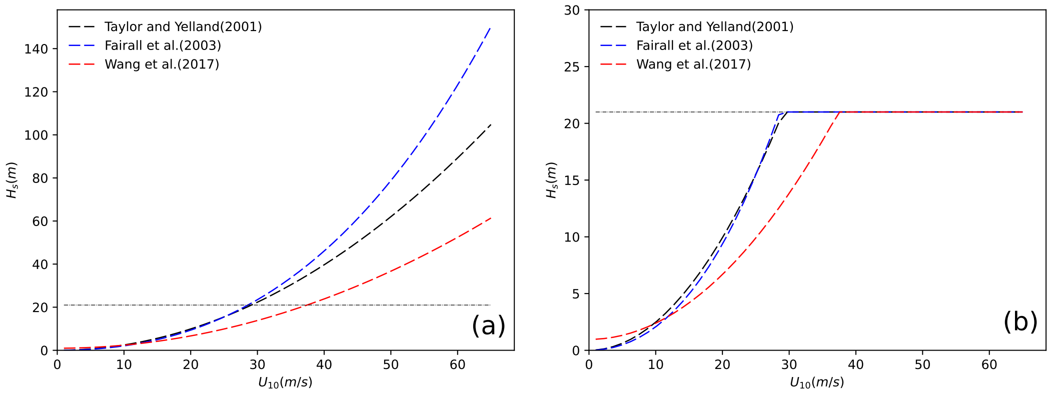

Figure 6. H_s versus U_{10} (**a**) without threshold and (**b**) with threshold from Taylor and Yelland [51], Fairall et al. [81], and Wang et al. [82]. The threshold of H_s = 21 m is shown as the thin dashed line.

5.2. Validation of the Proposed Parameterization

In order to show how sea foam affects our results, the comparison between the curves of our parameterization without the effect of sea foam (Equation (23)) and the field observations from Powell et al. [29] and Jarosz et al. [68] is presented in Figure 7. Figure 7a–c denotes the different relations from H_s estimated from Taylor and Yelland [51], Fairall et al. [81], and Wang et al. [82], respectively. For the curves of $\beta_* < 15.21$, δ has been converted to β_* using the $\delta - \beta_*$ relationship derived from *Toba's* [72] 3/2 power law (Equation (22)). From Figure 7, we can see that the curves of C_d from Equation (23) can not reproduce the decreasing of C_d at high winds. The effect of sea foam can be seen from the comparison between Figures 7 and 8.

Given that z_f in Equation (29) is taken as different values for field and laboratory conditions, we compared the new parameterization with field and laboratory observations separately. Figure 8 shows the comparison between C_d predicted by the new parameterization (Equation (29)) under different wave ages and the field observations from Powell et al. [29] and Jarosz et al. [68]. From Figure 8, we can see that C_d predicted by the new proposed parameterization using different H_s schemes are generally consistent. C_d increases with wind speed in the range of 0–30 m/s, the maximum values are reached at about 30∼35 m/s, then decreases at the wind speed about 35∼45 m/s under the effect of sea foam, for wind speed larger than 45 m/s, the values of C_d do not change much. By comparing Figures 7 and 8, the effect of sea foam is obvious, by adding the sea foam, our parameterization can reproduce the reduction of C_d at U_{10} > 30 m/s, which is closer to the observations.

Results from H_s schemes proposed by Taylor and Yelland [51] and Fairall et al. [81] (Figure 8a,b, respectively) do not show much differences, but the results from Wang et al. [82] (Figure 8c) are different from the other at low and moderate wind speeds, in which the values of C_d are larger than the other two, especially for the younger wave. The difference is caused by the intercept of the formula proposed by Wang et al. [82] (see Equation (32)), when U_{10} is close to zero, H_s still has an initial value, given that young wave fields generally do not correspond to low wind speeds; this difference is not obvious in practice.

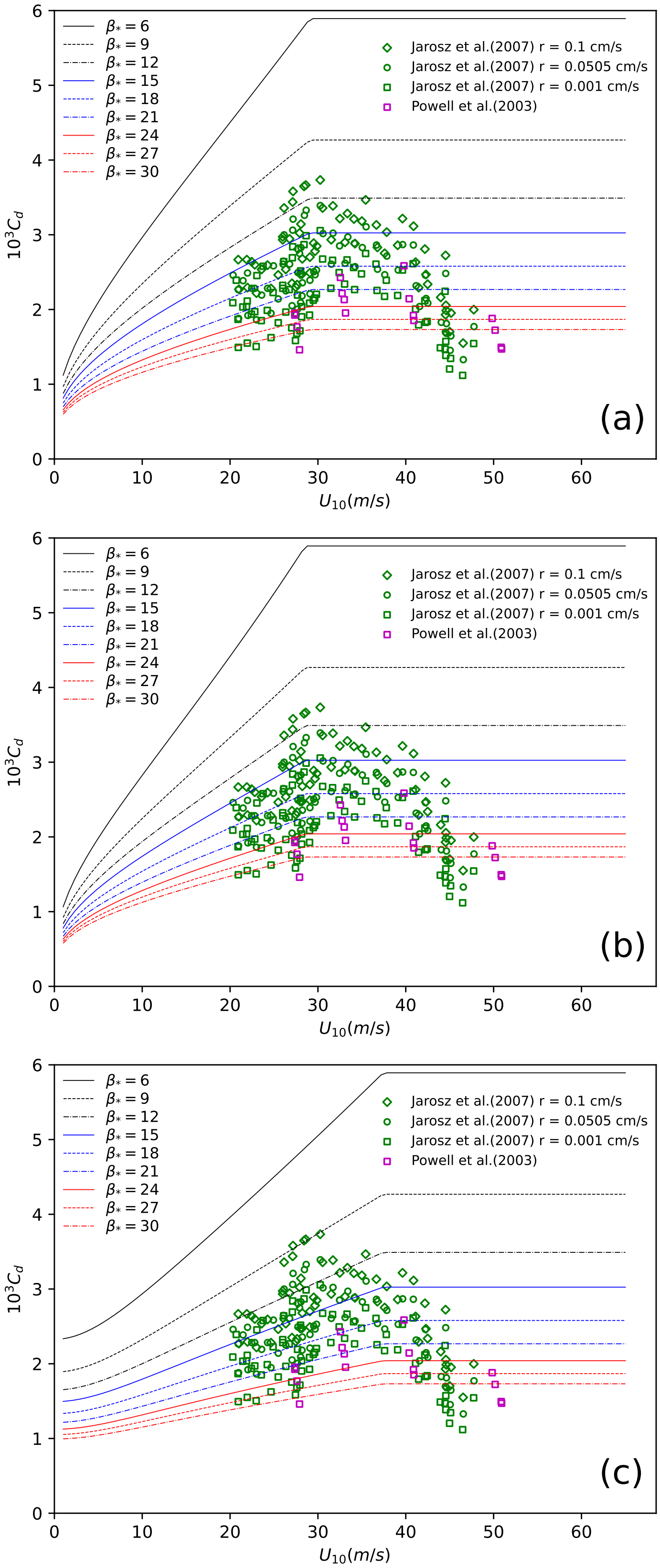

Figure 7. Comparison between C_d predicted by the new parameterization without the effect of sea foam (Equation (23)) under different wave ages using H_s estimated from (**a**) Taylor and Yelland [51]; (**b**) Fairall et al. [81]; and (**c**) Wang et al. [82] and the field observations.

The curves of the new proposed parameterization shown in Figure 8 can cover the range of the field observational data well, and the scatter of the observations can be explained as the effect of wave state. The reduction of C_d under high wind speeds is successfully reproduced by the new proposed parameterization, C_d predicted by the new proposed parameterization reach the maximum values in the wind range of 30∼35 m/s, which is consistent with the field measurements in Jarosz et al. [68] and Powell et al. [29]. The maximum value in Jarosz et al. [68] with the resistance coefficient of 0.1 cm/s ($\sim 3.7 \times 10^{-3}$) is close to the maximum value of $\beta_* = 9$ in Figure 8a,b, and is between $\beta_* = 9$ and $\beta_* = 6$ in Figure 8c. Furthermore, compared with the curves in Jarosz et al. [68] (cf Figures 2 and 3 therein), our parameterization provides C_d values for $U_{10} > 50$ m/s, while curves in Jarosz et al. [68] did not, considering that conditions with U_{10} larger than 50 m/s are common in tropical cyclones, our parameterization is suitable for the usage in tropical cyclone modeling and storm surge modeling. Since the simultaneous wave state was not measured by Jarosz et al. [68], we cannot compare the predictions of C_d with the observations directly.

Figure 9 shows the comparison between C_d predicted by the new parameterization under different wave ages and the laboratory observations from Donelan et al. [27] and Takagaki et al. [28]. The laboratory measurements do not show a decreasing trend under high wind speeds, their C_d tend to saturate at wind speeds larger than 35 m/s. The difference between the field and laboratory measurements can be expected due to significant differences in fetch [35]; in addition, in hurricane conditions, the wave field is dominated by swell generated in the high wind areas, but it will not be reproduced under laboratory conditions [83]. Consistent with the laboratory measurements, C_d predicted by the new parameterization also shows a saturation at $U_{10} > 40\,\mathrm{m/s}$, the saturation values of the observations match the predicted C_d well, both of them are very close to $C_d = 0.0024$. For $U_{10} < 30\,\mathrm{m/s}$, the values of observations concentrate near the curve of a larger wave age; considering that wave age is negative related to wind speed, and lower wind speed usually corresponds to a larger wave age, this result is reasonable. Observations from Donelan et al. [27] are slightly lower than that predicted by our parameterization, especially for MB and PM methods, this slightly difference is caused by the calculation method and the measuring instrument, i.e., the RS method uses the stress data directly measured from an x-film anemometer, the PM method uses wind speed data measured from the hot-film anemometry, and the MB method uses the bottom stress from DPIV and surface elevation from laser/line scan cameras to calculate C_d.

Although the proposed parameterization can reasonably explain the behavior of the observational data, it should be pointed out that the values predicted by the new parameterization have not been compared with the observational data directly due to the lack of simultaneous wave state measurements under high wind speed conditions. Thus, more field and laboratory experiments containing simultaneous wind and wave state measurements are needed to further verify the performance of the new parameterization, and to investigate the mechanism of momentum transfer across the air–sea interface.

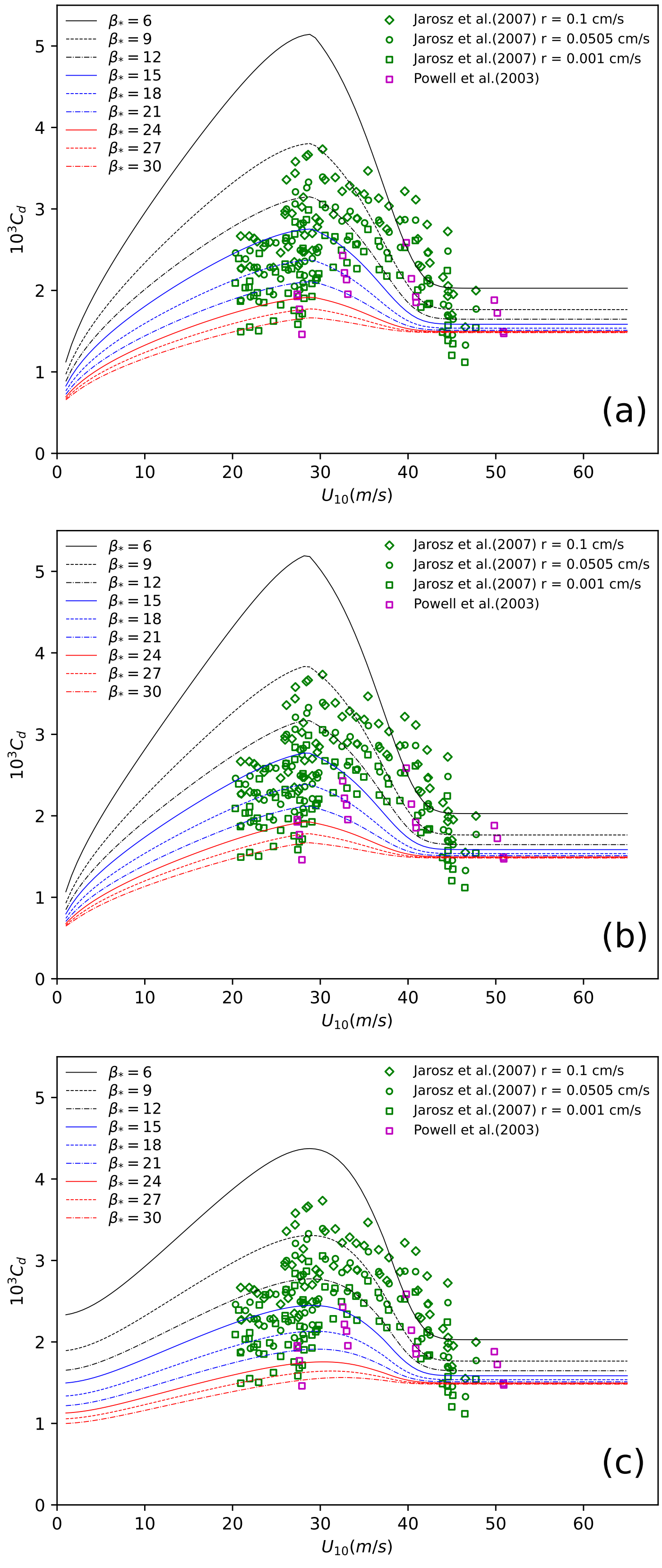

Figure 8. Comparison between C_d predicted by the new parameterization with the effect of sea foam (Equation (29)) under different wave ages using H_s estimated from (**a**) Taylor and Yelland [51]; (**b**) Fairall et al. [81]; and (**c**) Wang et al. [82] and the field observations.

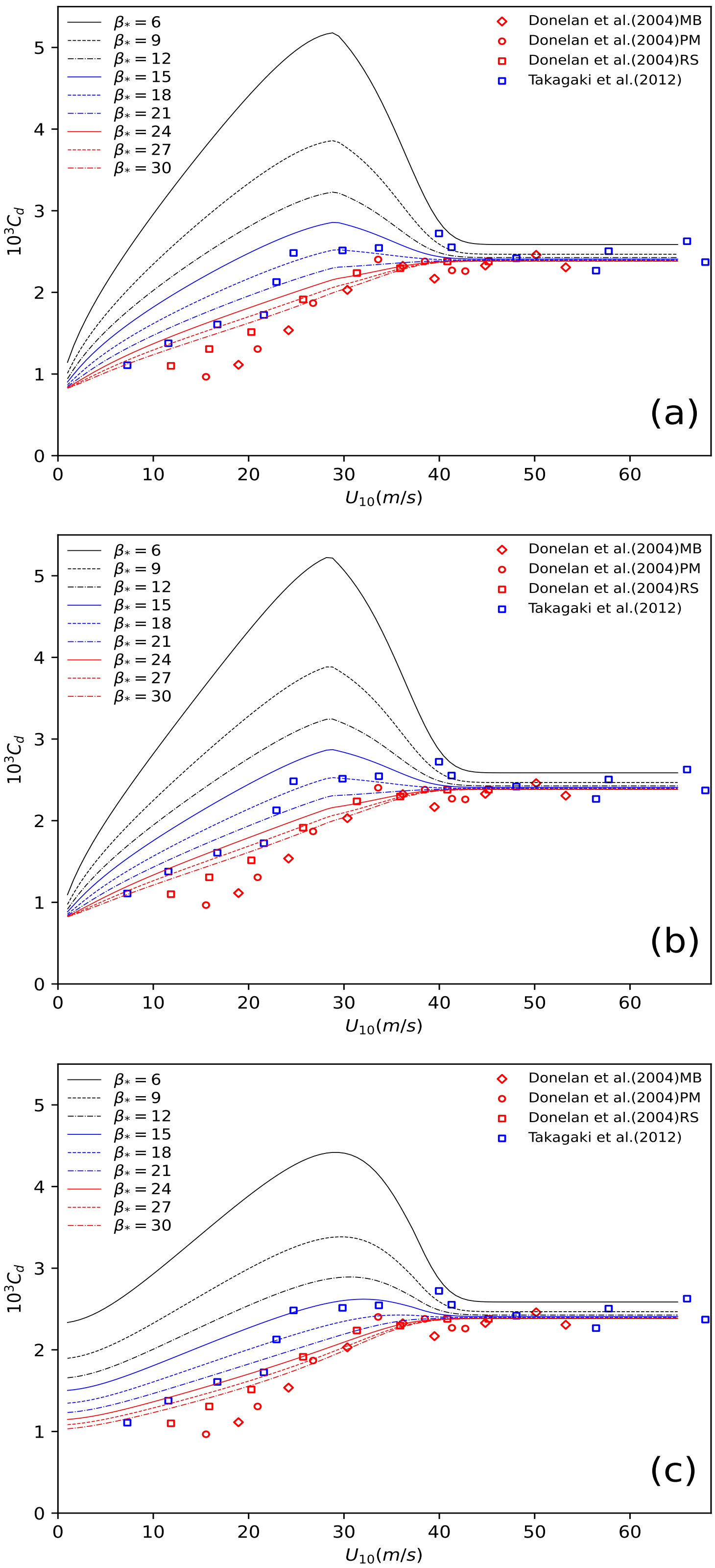

Figure 9. Comparison between C_d predicted by the new parameterization under different wave ages using H_s estimated from (**a**) Taylor and Yelland [51]; (**b**) Fairall et al. [81]; and (**c**) Wang et al. [82] and the laboratory observations.

5.3. Comparison with Other Parameterizations

In this section, the performance of our parameterization has been compared with three different parameterizations, these parameterizations have been proposed for the calculation of C_d in high wind speed conditions, and the saturation of C_d has been dealt with different method.

Based on the work of Powell [84] and Garratt [17], Luettich and Westerink [85] offered a formulation that divides the tropical cyclone into three sectors and calculated C_d accordingly; this formula has been used in the ADvanced CIRCulation (ADCIRC) storm surge model (here, we denote it as ADCIRC). For the right sector of a storm:

$$C_d = \begin{cases} (0.75 + 0.067U_{10}) \times 10^{-3}, & U_{10} \leq 35 \text{ m/s} \\ 0.0020 + \frac{(0.0030-0.0020)}{(45.0-35.0)}(U_{10} - 35.0), & 35 \text{ m/s} \leq U_{10} \leq 45 \text{ m/s} \\ 0.0030, & U_{10} > 45 \text{ m/s} \end{cases}, \quad (33)$$

for the rear sector of a storm:

$$C_d = \begin{cases} (0.75 + 0.067U_{10}) \times 10^{-3}, & U_{10} \leq 35 \text{ m/s} \\ 0.0020 + \frac{(0.0010-0.0020)}{(45.0-35.0)}(U_{10} - 35.0), & 35 \text{ m/s} \leq U_{10} \leq 45 \text{ m/s} \\ 0.0010, & U_{10} > 45 \text{ m/s} \end{cases}, \quad (34)$$

and for the left front sector of a storm:

$$C_d = \begin{cases} 0.0018, & U_{10} \leq 25 \text{ m/s} \\ 0.0018 + \frac{(0.0045-0.0018)}{(30.0-25.0)}(U_{10} - 25.0), & 25 \text{ m/s} \leq U_{10} \leq 30 \text{ m/s} \\ 0.0045 + \frac{(0.0010-0.0045)}{(45.0-30.0)}(U_{10} - 35.0), & 30 \text{ m/s} \leq U_{10} \leq 45 \text{ m/s} \\ 0.0010, & U_{10} > 45 \text{ m/s} \end{cases}. \quad (35)$$

Using more than 6000 near-surface flux measurements collected from low-flying aircrafts, Andreas proposed a parameterization for low-to-high winds (here, we denote it as A12):

$$u_* = 0.239 + 0.0433(U_{10} - 8.271) + [0.120(U_{10} - 8.271)^2 + 0.181]^{1/2}. \quad (36)$$

C_d can be calculated from $C_d = (\frac{u_*}{U_{10}})^2$.

According to the dependence of wind speed-C_d relation on swell, Holthuijsen et al. [80] proposed a parameterization for different swell conditions (here, we denote it as H12):

$$C_d \times 10^3 = min[a + b(\frac{U_{10}}{27.5})^c], d[1 - (\frac{U_{10}}{54.0})^e]. \quad (37)$$

For no swell, opposing swell, and following swell, a = 1.05, b = 1.25, c = 1.4, d = 2.3, and e = 10; for cross swell a = 0.7, b = 1.1, c = 6, d = 8.2, and e = 2.5.

The comparison between the above-mentioned three parameterizations and our new parameterizations, along with two field observations, are presented in Figure 10 because the curves of our parameterization only show a little difference for different H_s parameterization as shown in Figures 8 and 9, we only plot the curves based on the H_s parameterization of Wang et al. [82]. The results in Figure 10 show that the saturation of C_d are presented in different forms, all three forms of ADCIRC take C_d as constants for U_{10} > 45 m/s, but the values are different, the maximum value of C_d predicted by ADCIRC left front is about 0.0057, which is much larger than that observed in field experiments; another problem for ADCIRC parameterization is that their values of C_d are not continuous at their demarcation point of their formula, such as U_{10} = 30 m/s, U_{10} = 35 m/s, and U_{10} = 45 m/s, which are unreasonable physically. The curve of A12 is smooth, but the reduction of C_d at U_{10} > 35 m/s has not been reproduced by their formula. C_d predicted by H12 under cross swell conditions reaches a maximum value of about 0.0053 at $U_{10} \approx$ 35 m/s, then decreases rapidly, the predicted C_d is smaller than 0 when $U_{10} > 54$ m/s, this is also incorrect. In general, these three schemes have deficiencies in different aspects, our parameterization has presented the most reasonable results.

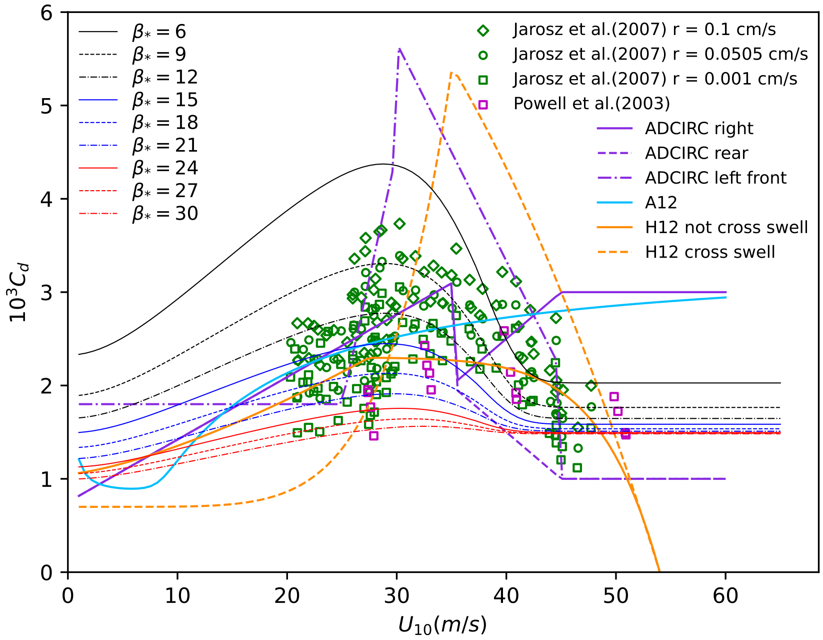

Figure 10. As in Figure 8c, but the curves of ADCIRC, A12, and H12 are plotted.

6. Conclusions

An accurate estimate of momentum transfer across the air–sea interface is vital for atmospheric, oceanic, and surface wave prediction models. Compared with parameterization of momentum flux based on wind speed, parameterization based on wave state can describe the nature of the air–sea interface more directly. Wave age ($\beta = c_p/U_{10}$, or $\beta_* = c_p/u_*$) and wave steepness ($\delta = H_s/L_p$) are two of the most frequently used parameters to describe the air–sea interface and the development of wind wave. Using eight observational datasets, the performances of two most widely used wave state related parameterizations: TY01 and DN03, are examined under various wave conditions. TY01 shows a better performance for the younger waves (smaller β_*), while DN03 is more suitable for wave fields with medium or large wave age. Hence, we use a combination of them to get a better performance under various wave conditions: for $\beta_* < 15.21$, TY01 is adopted; and, for $\beta_* \geq 15.21$, DN03 is adopted. The demarcation point $\beta_* = 15.21$ is selected from the $\delta - \beta_*$ relationship derived from *Toba's* [72] 3/2 power law (see Equation (22)). Considering that TY01 and DN03 were developed using observational data under low and moderate wind speed conditions ($U_{10} \leq 20$ m/s), the effect of sea foam was not included explicitly or implicitly in the proposing of TY01 and DN03. By introducing the effect of sea foam into the scheme presented in Section 3 (see Equation (23)), a new parameterization of sea surface roughness based on the wave state and sea foam is proposed (see Equation (29)).

C_d predicted by the new parameterization increases with wind speed in the range of 0∼30 m/s; the maximum values are reached at about 30∼35 m/s and then decrease at the wind speed about 35∼45 m/s under the effect of sea foam; its behavior is also supported by the field observations from [29,68]. The saturation values of C_d in laboratory measurements from [27,28] is also reproduced by the new parameterization.

Due to the vital role of wave state and sea foam on the momentum transfer across the air–sea interface, the new proposed sea surface roughness parameterization is suitable for the coupled atmosphere-ocean-wave modeling systems. Furthermore, as the effects of sea foam are included in the presented parameterization, it is also applicable for the modeling of some severe air–sea interaction activities accompanied with extreme winds, such as tropical cyclones, and the wave modeling of storm surge.

Finally, it should be emphasized that, due to the lack of simultaneous wave state measurements under high wind speed conditions, the values predicted by the new parameterization have not been compared with the observational data directly. Thus, more field and laboratory experiments containing simultaneous wind and wave state measurements, especially for high wind speed conditions, are needed to further verify the performance of the new parameterization, and to investigate the specific mechanism of air–sea interaction. However, although a direct comparison between the new parameterization with the observational data at high wind speeds is difficult, assessing it in the numerical weather prediction system is more realistic. It is our plan to implement the new parameterization in numerical models, including large-eddy simulations and coupled atmosphere-wave models, and to evaluate the performance of our parameterization from the model results.

Author Contributions: Conceptualization, D.S.; Methodology, D.S. and J.S.; Formal analysis and investigation, D.S., J.S., H.L., K.R. and X.L.; Writing—review and editing, D.S., H.L., and X.L. All authors have read and agreed to the published version of the manuscript.

Funding: This research was funded by the National Key R&D Program of China (2018YFB0203801) and the National Nature Science Foundation of China (41605070).

Institutional Review Board Statement: Not applicable.

Informed Consent Statement: Not applicable.

Data Availability Statement: The observational datasets used in this study are available in the corresponding literature at https://doi.org/10.1175/1520-0485(1996)026<1344:AMFOOS>2.0.CO;2 (accessed on 11 February 2021), https://doi.org/10.1029/2007JC004233 (accessed on 11 February 2021), https://doi.org/10.1080/07055900.1994.9649497 (accessed on 11 February 2021), https://doi.org/10.1175/1520-0485(1996)026<0808:OTDMIS>2.0.CO;2 (accessed on 11 February 2021), https://doi.org/10.1029/JC092iC12p13127 (accessed on 11 February 2021), https://doi.org/10.1023/A:1000336814021 (accessed on 11 February 2021), https://doi.org/10.1175/1520-0485(1998)028<1702:OTDOSS>2.0.CO;2 (accessed on 11 February 2021), https://doi.org/10.1175/2009JPO4127.1 (accessed on 11 February 2021), https://doi.org/10.1029/2004GL019460 (accessed on 11 February 2021), https://doi.org/10.1029/2012GL053988 (accessed on 11 February 2021), https://doi.org/10.1038/nature01481 (accessed on 11 February 2021), and https://doi.org/10.1126/science.1136466 (accessed on 11 February 2021).

Conflicts of Interest: The authors declare no conflict of interest. The funders had no role in the design of the study; in the collection, analyses, or interpretation of data; in the writing of the manuscript, or in the decision to publish the results.

References

1. Kumar, R.; Sandeepan, B.; Holland, D.M. Impact of different sea surface roughness on surface gravity waves using a coupled atmosphere–wave model: A case of Hurricane Isaac (2012). *Ocean Dyn.* **2020**, *70*, 421–433. [CrossRef]
2. Golbraikh, E.; Shtemler, Y.M. Momentum and heat transfer across the foam-covered air–sea interface in hurricanes. *Ocean Dyn.* **2020**, *70*, 683–692. [CrossRef]
3. Yousefi, K.; Veron, F.; Buckley, M.P. Momentum flux measurements in the airflow over wind-generated surface waves. *J. Fluid Mech.* **2020**, *895*. [CrossRef]
4. Bye, J.A.; Jenkins, A.D. Drag coefficient reduction at very high wind speeds. *J. Geophys. Res. Ocean.* **2006**, *111*. [CrossRef]
5. Priestley, C.H.B. *Turbulent Transfer in the Lower Atmosphere*; CSIRO: Canberra, Australia, 1959.
6. Lumley, J.; Panofsky, H. The structure of atmospheric turbulence. New York. Interscience Publ. MacPherson, J. y GA Isaac, 1977. Turbulent characteristics of some Canadian cumulus clouds. *J. Appl. Meteorx.* **1964**, *16*, 81–90.
7. Webb, E.K. Profile relationships: The log-linear range, and extension to strong stability. *Q. J. R. Meteorol. Soc.* **1970**, *96*, 67–90. [CrossRef]
8. Paulson, C.A. The mathematical representation of wind speed and temperature profiles in the unstable atmospheric surface layer. *J. Appl. Meteorol.* **1970**, *9*, 857–861. [CrossRef]
9. Grachev, A.A.; Andreas, E.L.; Fairall, C.W.; Guest, P.S.; Persson, P.O.G. SHEBA flux–profile relationships in the stable atmospheric boundary layer. *Bound.-Layer Meteorol.* **2007**, *124*, 315–333. [CrossRef]
10. Smith, S.D. Wind stress and heat flux over the ocean in gale force winds. *J. Phys. Oceanogr.* **1980**, *10*, 709–726. [CrossRef]

11. Smith, S.D.; Anderson, R.J.; Oost, W.A.; Kraan, C.; Maat, N.; De Cosmo, J.; Katsaros, K.B.; Davidson, K.L.; Bumke, K.; Hasse, L.; et al. Sea surface wind stress and drag coefficients: The HEXOS results. *Bound.-Layer Meteorol.* **1992**, *60*, 109–142. [CrossRef]
12. Geernaert, G.; Larsen, S.; Hansen, F. Measurements of the wind stress, heat flux, and turbulence intensity during storm conditions over the North Sea. *J. Geophys. Res. Ocean.* **1987**, *92*, 13127–13139. [CrossRef]
13. Edson, J.B.; Jampana, V.; Weller, R.A.; Bigorre, S.P.; Plueddemann, A.J.; Fairall, C.W.; Miller, S.D.; Mahrt, L.; Vickers, D.; Hersbach, H. On the exchange of momentum over the open ocean. *J. Phys. Oceanogr.* **2013**, *43*, 1589–1610. [CrossRef]
14. Guan, C.; Xie, L. On the linear parameterization of drag coefficient over sea surface. *J. Phys. Oceanogr.* **2004**, *34*, 2847–2851. [CrossRef]
15. Kondo, J. Air-sea bulk transfer coefficients in diabatic conditions. *Bound.-Layer Meteorol.* **1975**, *9*, 91–112. [CrossRef]
16. Smith, S.; Banke, E. Variation of the sea surface drag coefficient with wind speed. *Q. J. R. Meteorol. Soc.* **1975**, *101*, 665–673. [CrossRef]
17. Garratt, J. Review of drag coefficients over oceans and continents. *Mon. Weather Rev.* **1977**, *105*, 915–929. [CrossRef]
18. Wu, J. Wind-stress coefficients over sea surface near neutral conditions—A revisit. *J. Phys. Oceanogr.* **1980**, *10*, 727–740. [CrossRef]
19. Large, W.; Pond, S. Open ocean momentum flux measurements in moderate to strong winds. *J. Phys. Oceanogr.* **1981**, *11*, 324–336. [CrossRef]
20. Donelan, M.A. The dependence of the aerodynamic drag coefficient on wave parameters. In Proceedings of the First, International Conference on meteorological and Air–Sea Interaction of the Coastal Zone, The Hague, The Netherlands, 10–12 May 1982; American Meteorological Society: Boston, MA, USA, 1982; pp. 381–387.
21. Yelland, M.; Taylor, P.K. Wind stress measurements from the open ocean. *J. Phys. Oceanogr.* **1996**, *26*, 541–558. [CrossRef]
22. Vickers, D.; Mahrt, L. Fetch limited drag coefficients. *Bound.-Layer Meteorol.* **1997**, *85*, 53–79. [CrossRef]
23. Drennan, W.M.; Graber, H.C.; Donelan, M.A. Evidence for the effects of swell and unsteady winds on marine wind stress. *J. Phys. Oceanogr.* **1999**, *29*, 1853–1864. [CrossRef]
24. Toffoli, A.; Loffredo, L.; Le Roy, P.; Lefèvre, J.M.; Babanin, A. On the variability of sea drag in finite water depth. *J. Geophys. Res. Ocean.* **2012**, *117*. [CrossRef]
25. Bender, M.A.; Ginis, I.; Kurihara, Y. Numerical simulations of tropical cyclone-ocean interaction with a high-resolution coupled model. *J. Geophys. Res. Atmos.* **1993**, *98*, 23245–23263. [CrossRef]
26. Tolman, H.L.; Balasubramaniyan, B.; Burroughs, L.D.; Chalikov, D.V.; Chao, Y.Y.; Chen, H.S.; Gerald, V.M. Development and implementation of wind-generated ocean surface wave Modelsat NCEP. *Weather Forecast.* **2002**, *17*, 311–333. [CrossRef]
27. Donelan, M.; Haus, B.K.; Reul, N.; Plant, W.; Stiassnie, M.; Graber, H.C.; Brown, O.; Saltzman, E. On the limiting aerodynamic roughness of the ocean in very strong winds. *Geophys. Res. Lett.* **2004**, *31*. [CrossRef]
28. Takagaki, N.; Komori, S.; Suzuki, N.; Iwano, K.; Kuramoto, T.; Shimada, S.; Kurose, R.; Takahashi, K. Strong correlation between the drag coefficient and the shape of the wind sea spectrum over a broad range of wind speeds. *Geophys. Res. Lett.* **2012**, *39*. [CrossRef]
29. Powell, M.D.; Vickery, P.J.; Reinhold, T.A. Reduced drag coefficient for high wind speeds in tropical cyclones. *Nature* **2003**, *422*, 279–283. [CrossRef]
30. Zijlema, M.; Van Vledder, G.P.; Holthuijsen, L. Bottom friction and wind drag for wave models. *Coast. Eng.* **2012**, *65*, 19–26. [CrossRef]
31. Green, B.W.; Zhang, F. Impacts of air–sea flux parameterizations on the intensity and structure of tropical cyclones. *Mon. Weather Rev.* **2013**, *141*, 2308–2324. [CrossRef]
32. Chen, Y.; Zhang, F.; Green, B.W.; Yu, X. Impacts of ocean cooling and reduced wind drag on Hurricane Katrina (2005) based on numerical simulations. *Mon. Weather Rev.* **2018**, *146*, 287–306. [CrossRef]
33. Moon, I.J.; Kwon, J.I.; Lee, J.C.; Shim, J.S.; Kang, S.K.; Oh, I.S.; Kwon, S.J. Effect of the surface wind stress parameterization on the storm surge modeling. *Ocean Model.* **2009**, *29*, 115–127. [CrossRef]
34. Bryant, K.M.; Akbar, M. An exploration of wind stress calculation techniques in hurricane storm surge modeling. *J. Mar. Sci. Eng.* **2016**, *4*, 58. [CrossRef]
35. Troitskaya, Y.I.; Sergeev, D.; Kandaurov, A.; Baidakov, G.; Vdovin, M.; Kazakov, V. Laboratory and theoretical modeling of air–sea momentum transfer under severe wind conditions. *J. Geophys. Res. Ocean.* **2012**, *117*. [CrossRef]
36. Takagaki, N.; Komori, S.; Suzuki, N.; Iwano, K.; Kurose, R. Mechanism of drag coefficient saturation at strong wind speeds. *Geophys. Res. Lett.* **2016**, *43*, 9829–9835. [CrossRef]
37. Komori, S.; Iwano, K.; Takagaki, N.; Onishi, R.; Kurose, R.; Takahashi, K.; Suzuki, N. Laboratory measurements of heat transfer and drag coefficients at extremely high wind speeds. *J. Phys. Oceanogr.* **2018**, *48*, 959–974. [CrossRef]
38. Makin, V.K. A note on the drag of the sea surface at hurricane winds. *Bound.-Layer Meteorol.* **2005**, *115*, 169–176. [CrossRef]
39. Troitskaya, Y.; Ezhova, E.; Soustova, I.; Zilitinkevich, S. On the effect of sea spray on the aerodynamic surface drag under severe winds. *Ocean Dyn.* **2016**, *66*, 659–669. [CrossRef]
40. Rastigejev, Y.; Suslov, S.A. E–ε model of spray-laden near-sea atmospheric layer in high wind conditions. *J. Phys. Oceanogr.* **2014**, *44*, 742–763. [CrossRef]
41. Kudryavtsev, V.N.; Makin, V.K. Aerodynamic roughness of the sea surface at high winds. *Bound.-Layer Meteorol.* **2007**, *125*, 289–303. [CrossRef]

42. Kukulka, T.; Hara, T.; Belcher, S.E. A model of the air–sea momentum flux and breaking-wave distribution for strongly forced wind waves. *J. Phys. Oceanogr.* **2007**, *37*, 1811–1828. [CrossRef]
43. Liu, B.; Guan, C.; Xie, L. The wave state and sea spray related parameterization of wind stress applicable from low to extreme winds. *J. Geophys. Res. Ocean.* **2012**, *117*. [CrossRef]
44. Moon, I.J.; Ginis, I.; Hara, T. Effect of surface waves on air–sea momentum exchange. Part II: Behavior of drag coefficient under tropical cyclones. *J. Atmos. Sci.* **2004**, *61*, 2334–2348. [CrossRef]
45. Toba, Y.; Iida, N.; Kawamura, H.; Ebuchi, N.; Jones, I.S. Wave dependence of sea-surface wind stress. *J. Phys. Oceanogr.* **1990**, *20*, 705–721. [CrossRef]
46. Donelan, M.A.; Dobson, F.W.; Smith, S.D.; Anderson, R.J. On the dependence of sea surface roughness on wave development. *J. Phys. Oceanogr.* **1993**, *23*, 2143–2149. [CrossRef]
47. Hwang, P.A. Temporal and spatial variation of the drag coefficient of a developing sea under steady wind-forcing. *J. Geophys. Res. Ocean.* **2005**, *110*. [CrossRef]
48. Zhao, D.; Li, M. Dependence of wind stress across an air–sea interface on wave states. *J. Oceanogr.* **2019**, *75*, 207–223. [CrossRef]
49. Drennan, W.M.; Graber, H.C.; Hauser, D.; Quentin, C. On the wave age dependence of wind stress over pure wind seas. *J. Geophys. Res. Ocean.* **2003**, *108*. [CrossRef]
50. Anctil, F.; Donelan, M. Air–water momentum flux observations over shoaling waves. *J. Phys. Oceanogr.* **1996**, *26*, 1344–1353. [CrossRef]
51. Taylor, P.K.; Yelland, M.J. The dependence of sea surface roughness on the height and steepness of the waves. *J. Phys. Oceanogr.* **2001**, *31*, 572–590. [CrossRef]
52. Drennan, W.M.; Taylor, P.K.; Yelland, M.J. Parameterizing the sea surface roughness. *J. Phys. Oceanogr.* **2005**, *35*, 835–848. [CrossRef]
53. Olabarrieta, M.; Warner, J.C.; Armstrong, B.; Zambon, J.B.; He, R. Ocean–atmosphere dynamics during Hurricane Ida and Nor'Ida: An application of the coupled ocean–atmosphere–wave–sediment transport (COAWST) modeling system. *Ocean Model.* **2012**, *43*, 112–137. [CrossRef]
54. Soloviev, A.V.; Lukas, R.; Donelan, M.A.; Haus, B.K.; Ginis, I. The air–sea interface and surface stress under tropical cyclones. *Sci. Rep.* **2014**, *4*, 5306. [CrossRef] [PubMed]
55. Golbraikh, E.; Shtemler, Y.M. Foam input into the drag coefficient in hurricane conditions. *Dyn. Atmos. Ocean.* **2016**, *73*, 1–9. [CrossRef]
56. Anctil, F.; Donelan, M.A.; Drennan, W.M.; Graber, H.C. Eddy-correlation measurements of air–sea fluxes from a discus buoy. *J. Atmos. Ocean. Technol.* **1994**, *11*, 1144–1150. [CrossRef]
57. Anderson, R. A study of wind stress and heat flux over the open ocean by the inertial-dissipation method. *J. Phys. Oceanogr.* **1993**, *23*, 2153–2161. [CrossRef]
58. Young, I.R.; Banner, M.L.; Donelan, M.A.; McCormick, C.; Babanin, A.V.; Melville, W.K.; Veron, F. An integrated system for the study of wind-wave source terms in finite-depth water. *J. Atmos. Ocean. Technol.* **2005**, *22*, 814–831. [CrossRef]
59. Babanin, A.V.; Makin, V.K. Effects of wind trend and gustiness on the sea drag: Lake George study. *J. Geophys. Res. Ocean.* **2008**, *113*. [CrossRef]
60. Dobson, F.W.; Smith, S.D.; Anderson, R.J. Measuring the relationship between wind stress and sea state in the open ocean in the presence of swell. *Atmosphere-Ocean* **1994**, *32*, 237–256. [CrossRef]
61. Drennan, W.M.; Donelan, M.; Terray, E.; Katsaros, K. Oceanic turbulence dissipation measurements in SWADE. *J. Phys. Oceanogr.* **1996**, *26*, 808–815. [CrossRef]
62. Donelan, M. The air–sea momentum flux in mixed wind sea and swell conditions. *J. Phys. Oceanogr.* **1997**, *27*, 2087–2099. [CrossRef]
63. Janssen, J. Does wind stress depend on sea-state or not?–A statistical error analysis of Hexmax data. *Bound.-Layer Meteorol.* **1997**, *83*, 479–503. [CrossRef]
64. Johnson, H.; Højstrup, J.; Vested, H.; Larsen, S.E. On the dependence of sea surface roughness on wind waves. *J. Phys. Oceanogr.* **1998**, *28*, 1702–1716. [CrossRef]
65. Romero, L.; Melville, W.K. Airborne observations of fetch-limited waves in the Gulf of Tehuantepec. *J. Phys. Oceanogr.* **2010**, *40*, 441–465. [CrossRef]
66. Brown, E.N.; Friehe, C.; Lenschow, D. The use of pressure fluctuations on the nose of an aircraft for measuring air motion. *J. Clim. Appl. Meteorol.* **1983**, *22*, 171–180. [CrossRef]
67. Carter, D. Prediction of wave height and period for a constant wind velocity using the JONSWAP results. *Ocean Eng.* **1982**, *9*, 17–33. [CrossRef]
68. Jarosz, E.; Mitchell, D.A.; Wang, D.W.; Teague, W.J. Bottom-up determination of air–sea momentum exchange under a major tropical cyclone. *Science* **2007**, *315*, 1707–1709. [CrossRef]
69. Krogstad, H.E.; Wolf, J.; Thompson, S.P.; Wyatt, L.R. Methods for intercomparison of wave measurements. *Coast. Eng.* **1999**, *37*, 235–257. [CrossRef]
70. Donelan, M.A. Air-sea interaction. *Sea* **1990**, *9*, 239–292.

71. Ardhuin, F.; Rogers, E.; Babanin, A.V.; Filipot, J.F.; Magne, R.; Roland, A.; Van Der Westhuysen, A.; Queffeulou, P.; Lefevre, J.M.; Aouf, L.; et al. Semiempirical dissipation source functions for ocean waves. Part I: Definition, calibration, and validation. *J. Phys. Oceanogr.* **2010**, *40*, 1917–1941. [CrossRef]
72. Toba, Y. Local balance in the air–sea boundary processes. *J. Oceanogr.* **1972**, *28*, 109–120. [CrossRef]
73. Ebuchi, N.; Toba, Y.; Kawamura, H. Statistical study on the local equilibrium between wind and wind waves by using data from ocean data buoy stations. *J. Oceanogr.* **1992**, *48*, 77–92. [CrossRef]
74. Guan, C.; Sun, Q. Analyses of wind wave growth relations and their support to the 3/2 power law. *J. Ocean Univ. Qingdao* **2001**, *31*, 633–639.
75. Wen, S.; Zhang, D.; Guo, P.F.; Chen, B. Parameters in wind-wave frequency spectra and their bearings on spectrum forms and growth. *Acta Oceanol. Sin* **1989**, *8*, 15–39.
76. Goda, Y. Investigation of the statistical properties of sea waves with field and simulation data. *Rept. Port Harb. Res. Inst.* **1974**, *13*, 3–37.
77. Donelan, M.; Drennan, W. Direct field measurements of the flux of carbon dioxide. *Air-Water Gas Transf.* **1995**, *677*, 683.
78. Hauser, D.; Branger, H.; Bouffies-Cloché, S.; Despiau, S.; Drennan, W.; Dupuis, H.; Durand, P.; Durrieu de Madron, X.; Estournel, C.; Eymard, L.; et al. The FETCH experiment: An overview. *J. Geophys. Res. Ocean.* **2003**, *108*. [CrossRef]
79. Donelan, M.A.; Madsen, N.; Kahma, K.K.; Tsanis, I.K.; Drennan, W.M. Apparatus for atmospheric surface layer measurements over waves. *J. Atmos. Ocean. Technol.* **1999**, *16*, 1172–1182. [CrossRef]
80. Holthuijsen, L.H.; Powell, M.D.; Pietrzak, J.D. Wind and waves in extreme hurricanes. *J. Geophys. Res. Ocean.* **2012**, *117*. [CrossRef]
81. Fairall, C.W.; Bradley, E.F.; Hare, J.; Grachev, A.A.; Edson, J.B. Bulk parameterization of air–sea fluxes: Updates and verification for the COARE algorithm. *J. Clim.* **2003**, *16*, 571–591. [CrossRef]
82. Wang, C.; Fei, J.; Ding, J.; Hu, R.; Huang, X.; Cheng, X. Development of a new significant wave height and dominant wave period parameterization scheme. *Ocean Eng.* **2017**, *135*, 170–182. [CrossRef]
83. Young, I. A review of the sea state generated by hurricanes. *Mar. Struct.* **2003**, *16*, 201–218. [CrossRef]
84. Powell, M. Final report to the NOAA Joint Hurricane Testbed: Drag coefficient distribution and wind speed dependence in tropical cyclones. *NOAA Hurric. Res. Div.* **2007**. Available online: https://www.nhc.noaa.gov/jht/05-07reports/final_Powell_JHT07.pdf (accessed on 11 February 2021).
85. Luettich, R.; Westerink, J. ADCIRC: A (Parallel) Advanced Circulation Model for Oceanic, Coastal and Estuarine Waters. Users Manual. 2000. Available online: http://www.marine.unc.edu/C_CATS/adcirc/adcirc.htm (accessed on 11 February 2021).